Theoretical study on the massively augmented electro-osmotic water transport in polyelectrolyte brush functionalized nanoslits

Vishal Sankar Sivasankar, Sai Ankit Etha, Harnoor Singh Sachar, and Siddhartha Das *
Department of Mechanical Engineering, University of Maryland, College Park, Maryland 20742, USA

(Received 21 February 2020; revised 24 April 2020; accepted 8 June 2020; published 8 July 2020)

We demonstrate that functionalizing nanoslits with *p*H-responsive polyelectrolyte brushes can lead to extremely fast electro-osmotic (EOS) water transport, where the maximum centreline velocity and the volume flow rate can be an order of magnitude larger than these quantities in identically charged brush-free nanochannels for a wide range of system parameters. Such an enhancement is most remarkable given that the brushes have been known to retard the transport by imparting additional drag on the fluid flow. We argue that this enhancement stems from the localization of the charge density of the brush-induced electric double layer (and, hence, the EOS body force) away from the nanochannel wall (or the location of the wall-induced drag force). This ensures a much larger impact of the EOS body force triggering such fast water transport. Finally, the calculated flux values for the present brush-grafted nanochannels are found to be significantly larger than those for a wide range of nanofluidic membranes and channels, suggesting that the brush functionalization can be considered as a mechanism for enabling such superfast nanofluidic transport.

DOI: 10.1103/PhysRevE.102.013103

I. INTRODUCTION

Nanofluidic transport of liquids and ions [1–3] has been critical to a large number of disciplines ranging from energy generation, conversion, and utilization [4,5], sensing and separation [6,7], and gating of ion and liquids [8,9] to the understanding of the behavior of biological systems for developing biomimetic and bioinspired applications [10,11]. Very often, these applications necessitate modifying the properties and/or working principles of these nanochannels. Grafting the nanochannels with polyelectrolyte (PE) brushes that are sensitive to the environmental stimuli has served as one of the most popular techniques for modifying the nanochannel functionality, enabling applications such as ion and biosensing [12,13], fabrication of ionic diodes [14] and current rectifiers [15,16], etc. Most of these applications of the PE-brush-grafted nanochannels rely on the brush-induced alteration of the ionic current and are aided by the fact that the corresponding liquid transport is severely weakened due to the brush-induced additional drag force [17]. Such a reduction in liquid transport in micro- and nanochannels by grafting the channel walls with polymer or PE molecules is a well-documented phenomenon. For example, Bruin *et al.*, in their experimental study, reported a decrease in the electro-osmotic (EOS) flow in fused-silica capillaries with walls grafted with γ-glycidoxypropyltrimethoxy-silane and polyethylene glycol [18]. Fung and Yeung showed that the dynamic coating of polyethylene oxide (PEO) in bare-silica capillary columns was able to significantly reduce the EOS flow, which in turn enabled high-speed DNA sequencing [19]. A thorough study by Monteferrante *et al.* [20] combined experiments and theory to clearly establish that liquid flow velocity is significantly reduced in a capillary coated with a copolymer consisting of N,N-dimethylacrylamide (DMA), glycidyl methacrylate (GMA), 3-(trimethoxysilyl) propyl methacrylate (MAPS), and N,N-dimethyl aminoethyl acrylamide: they associated this velocity reduction to the large frictional forces imparted by the grafted polymer molecules. In addition to these experimental studies, there has been a plethora of simulation studies that employ sophisticated molecular dynamics (MD) simulations and establish such a significant flow reduction in nanochannels grafted with polymer or PE molecules and brushes due to the enhanced drag force imparted by these polymer molecules and brushes on the fluid flow [21–25].

In this paper, we describe a complete paradigm reversal in the context of the liquid transport in the PE brush-grafted nanochannels. We establish a wide range of parameter space where the grafting of nanochannels with *p*H-responsive, backbone-charged PE brushes can ensure an electro-osmotic (EOS) water transport that is much more augmented as compared to that in equally charged, brush-free nanochannels. Such superfast water transport manifests as, for some parameter combinations, channel centreline velocities and volume flow rates in brush-grafted nanochannels that are an order of magnitude larger than those for the similarly charged brush-free nanochannels. The brushes ensure that the effective center of the charge is away from the nanochannel wall, which implies that the effective center of the charge density of the brush-induced electric double layer (EDL) is also away from the wall. As a consequence, when an external axial electric field is employed to drive an EOS flow, the EOS body force (resulting from the interaction of this EDL charge density and the applied electric field) is localized away from the nanochannel wall (see Fig. 1). Therefore, there is a spatial difference in the location of the EOS body force and the wall-induced drag. Such a difference augments the influence of the EOS body force, which in turn induces, particularly for

* sidd@umd.edu

 ©2020 American Physical Society

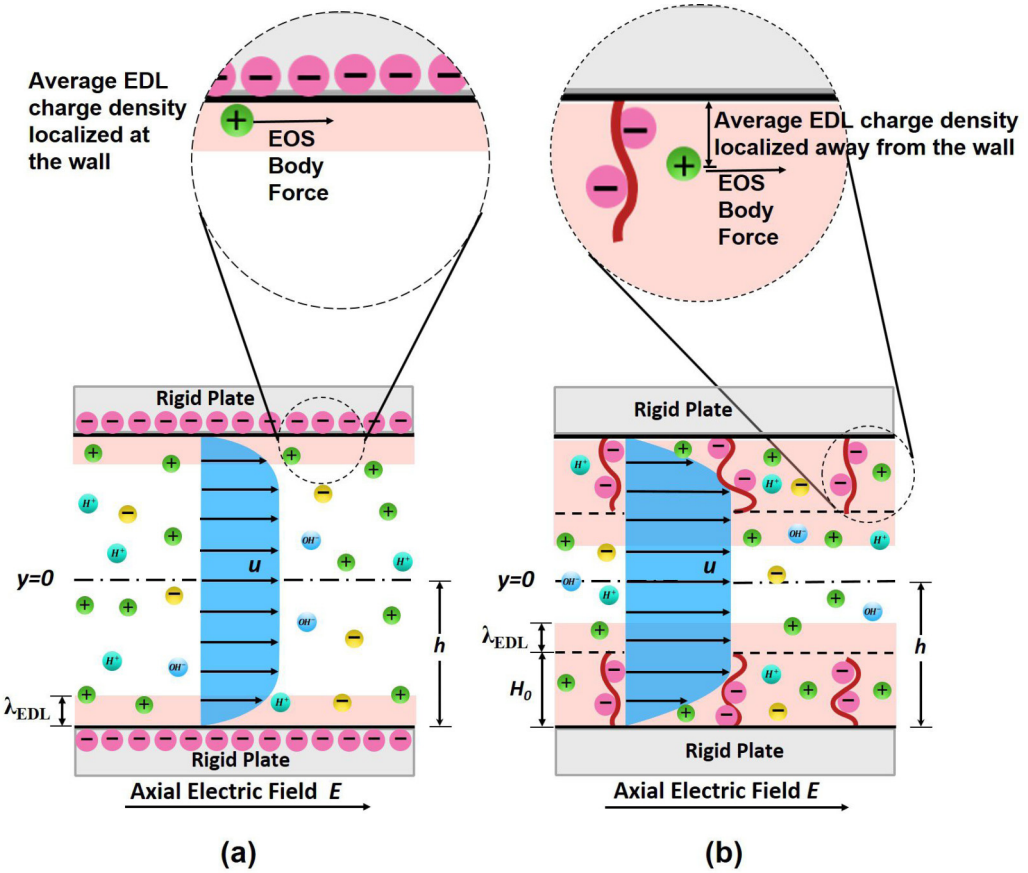

FIG. 1. Schematic comparing the EOS transport (due to the axial electric field) in (a) brush-free and (b) brush-grafted nanochannel. The brushes enforce the localization of the EDL charge density away from the wall enforcing the EOS body force to be localized away from the wall (location of the drag force). Here, λ_{EDL} denotes the EDL thickness.

conditions that increase the brush height, such an augmentation of the velocity field in comparison to that in the similarly charged brush-free nanochannels.

In a series of previous studies [26–29], we have established such EDL-localization-induced enhanced electrokinetic transport in nanochannels grafted with *end-charged PE brushes*. However, these studies did not manifest such massive augmentation in the flow field as they overestimated the drag (particularly for the tall brushes) from the brushes modeled using the simplistic Alexander–de Gennes model [30–32] that assumes a uniform monomer distribution. On the other hand, the present study considers a much more rigorous augmented strong stretching theory (SST) description of the PE brushes [33,34], which ensures a much larger monomer density at near-wall, low-velocity locations [33,34] leading to a smaller overall drag contribution (the local brush-induced drag force is proportional to the local fluid velocity and the drag coefficient is proportional to the square of the monomer density) from the brushes. Therefore, we can infer that the present study is different from the study of Chen and Das [26] in two critical aspects. First, the present study considers a much more realistic system (a fully backbone-charged PE brush as compared to an end-charged brush) and provides a significantly more rigorous description (augmented SST model [33,34] instead of the simplistic Alexander–de Gennes model [30–32]) of the PE brushes in modeling the EOS transport in brush-grafted nanochannels. Second, this more rigorous description of the PE brushes ensures that we do not overestimate the PE-brush-imparted drag force that occurs when the Alexander–de Gennes model, which considers a uniform monomer distribution, is employed to describe the PE brushes. Under such circumstances, we establish that in the presence of the experimentally realizable values of the applied axial electric fields ($10^4 - 5\times10^4$ V m^{-1}) [35], the EOS water flux values obtained for the present case of the PE-brush-grafted nanochannels can be significantly larger than the flux values obtained for nanochannel-, nanopassage-, or nanotube-based membranes [36–47] and nanofluidic systems [48–50] and less than one order of magnitude smaller than the tremendously high fluxes observed in graphene nanochannels and carbon nanotubes [51,52].

II. THEORY

We consider a nanochannel of height $2h$ ($-h \leqslant y \leqslant h$) grafted with *p*H-responsive, backbone-charged PE brushes [see Fig. 1(b)]. This section first provides the model to describe the equilibrium configuration of PE brushes and the brush-induced EDL electrostatics. Subsequently, we use this information to obtain the steady and fully developed EOS flow field in the PE-brush-grafted nanochannel.

A. Equilibrium configuration of PE brushes and the brush-induced EDL electrostatics: Theoretical model

The brushes are modeled using our recently developed augmented strong stretching theory (SST) [33,34] that extends the existing SST for the PE brushes [53,54] by accounting for the effects of the PE excluded volume interactions and a more generic mass action law. In this theory, the equilibrium configuration of the PE brushes and the equilibrium electrostatics of the brush-induced EDL are obtained by minimizing the total free energy of a given brush molecule that consists of the elastic, excluded volume, electrostatic, and ionization energies of the brush and the electrostatic energy of the brush-induced EDL. Here we provide a brief overview of this theoretical model by summarizing the key equations. For a more detailed step-by-step derivation of these different equations, we encourage the readers to kindly see our previous studies [33,34].

The calculations are based on minimizing the total energy functional (F) of the PE brush system. F therefore consists of the elastic ($F_{\rm els}$), excluded volume ($F_{\rm EV}$), electrostatic ($F_{\rm elec}$), and ionization ($F_{\rm ion}$) free energies of a PE brush molecule and the electrostatic energy of the EDL ($F_{\rm EDL}$) induced by this brush. Therefore,

$$F = F_{\rm els} + F_{\rm EV} + F_{\rm elec} + F_{\rm ion} + F_{\rm EDL}. \tag{1}$$

Due to symmetry, we shall only consider the bottom half of the nanochannel in our subsequent calculations. Following Zhulina *et al.* [55], therefore, we can express

$$\frac{F_{\rm els}}{k_BT} = \frac{3}{2pa^2}\int_{-h}^{-h+H} g(y')dy' \int_{-h}^{y'} E(y,y')dy, \tag{2}$$

$$\frac{F_{\rm EV}}{k_BT} = \frac{1}{\sigma a^3}\int_{-h}^{-h+H} f_{\rm conc}[\phi(y)]dy. \tag{3}$$

In the above equations, k_BT, p, a, H, and $\sigma \sim \frac{1}{\ell^2}$ (ℓ is the lateral separation between the adjacent PE brushes), respectively, represent the thermal energy, chain rigidity, Kuhn length, brush height, and PE-brush-grafting density. Also, $\phi(y)$ and $f_{\rm conc}[\phi(y)]$ ($\approx \nu\phi^2 + \omega\phi^3$), respectively, denote the dimensionless monomer distribution profile of a PE chain and the nondimensionalized per unit-volume free energy associated with the excluded volume interactions. Also, $E(y,y') = \frac{dy}{dn}$ expresses chain stretching (for a chain whose end is at y') at a location y and $g(y')$ (the normalized chain end distribution function) is expressed as

$$\int_{-h}^{-h+H} g(y')dy' = 1. \tag{4}$$

Next, following [56], $F_{\rm elec} + F_{\rm EDL}$ can be expressed as

$$\begin{aligned}\frac{F_{\rm elec}}{k_BT} + \frac{F_{\rm EDL}}{k_BT} &= \frac{1}{\sigma k_BT}\int_{-h}^{0}\left[-\frac{\epsilon_0\epsilon_r}{2}\left|\frac{d\psi}{dy}\right|^2 + e\psi(n_+ - n_- + n_{H^+} - n_{OH^-})\right]dy - \frac{1}{\sigma k_BT}\int_{-h}^{-h+H}[e\psi n_{A^-} - \phi]dy \\ &+ \frac{1}{\sigma}\int_{-h}^{0}\left\{n_+\left[\ln\left(\frac{n_+}{n_{+,\infty}}\right) - 1\right] + n_-\left[\ln\left(\frac{n_-}{n_{-,\infty}}\right) - 1\right] + n_{H^+}\left[\ln\left(\frac{n_{H^+}}{n_{H^+,\infty}}\right) - 1\right]\right. \\ &\left. + n_{OH^-}\left[\ln\left(\frac{n_{OH^-}}{n_{OH^-,\infty}}\right) - 1\right] + (n_{+,\infty} + n_{-,\infty} + n_{H^+,\infty} + n_{OH^-,\infty})\right\}dy,\end{aligned} \tag{5}$$

where ψ is the electrostatic potential, n_i and $n_{i,\infty}$ ($=10^3 N_A c_{i,\infty}$, where $c_{i,\infty}$ and N_A are the bulk concentration of ion i in Molars, and Avagadro number, respectively) are the number density and bulk number density for ion i (where $i = \pm$, H^+, OH^-), e is the charge of an electron, and ϵ_0 and ϵ_r are the permittivity of free space and relative permittivity of the solution, respectively.

Here we consider a pH-responsive PE brush that acquires charges by ionization through an acidlike dissociation process with HA producing H^+ and A^- ions (with K_a being the ionization constant for the reaction). The number density of these A^- ions is given by n_{A^-}. Accordingly, we can express $F_{\rm ion}$ as

$$\frac{F_{\rm ion}}{k_BT} = \frac{1}{\sigma a^3}\int_{-h}^{-h+H}\phi\left[\left(1 - \frac{n_{A^-}}{\gamma}\right)\ln\left(1 - \frac{n_{A^-}}{\gamma}\right) + \frac{n_{A^-}}{\gamma}\ln\left(\frac{n_{A^-}}{\gamma}\right) + \frac{n_{A^-}}{\gamma}\ln\left(\frac{n_{H^+,\infty}}{K_a'}\right)\right]dy, \tag{6}$$

where $K_a' = 10^3 N_A K_a$, $n_{H^+,\infty} = 10^3 N_A c_{H^+,\infty}$ ($c_{H^+,\infty}$ is the bulk concentration of the H^+ ions in Molars, which is related to bulk pH or $p\mathrm{H}_\infty$ as $c_{H^+,\infty} = 10^{-p\mathrm{H}_\infty}$), and γ ($1/m^3$) is the density of polyelectrolyte chargeable sites (PCS).

Using Eqs. (2), (3), (5), and (6) in Eq. (1), we can finally get the full expression for the free energy as

$$\begin{aligned}\frac{F}{k_BT} &= \frac{3}{2pa^2}\int_{-h}^{-h+H} g(y')dy' \int_{-h}^{y'} E(y,y')dy + \frac{1}{\sigma a^3}\int_{-h}^{-h+H} f_{\rm conc}[\phi(y)]dy + \frac{1}{\sigma k_BT}\int_{-h}^{0}\left[-\frac{\epsilon_0\epsilon_r}{2}\left|\frac{d\psi}{dy}\right|^2\right. \\ &\left. + e\psi(n_+ - n_- + n_{H^+} - n_{OH^-})\right]dy - \frac{1}{\sigma k_BT}\int_{-h}^{-h+H}[e\psi n_{A^-} - \phi]dy + 1/\sigma\int_{-h}^{0}\left\{n_+\left[\ln\left(\frac{n_+}{n_{+,\infty}}\right) - 1\right]\right. \\ &\left. + n_-\left[\ln\left(\frac{n_-}{n_{-,\infty}}\right) - 1\right] + n_{H^+}\left[\ln\left(\frac{n_{H^+}}{n_{H^+,\infty}}\right) - 1\right] + n_{OH^-}\left[\ln\left(\frac{n_{OH^-}}{n_{OH^-,\infty}}\right) - 1\right] + (n_{+,\infty} + n_{-,\infty} + n_{H^+,\infty} + n_{OH^-,\infty})\right\}dy \\ &+ \frac{1}{\sigma a^3}\int_{-h}^{-h+H}\phi\left[\left(1 - \frac{n_{A^-}}{\gamma}\right)\ln\left(1 - \frac{n_{A^-}}{\gamma}\right) + \frac{n_{A^-}}{\gamma}\ln\left(\frac{n_{A^-}}{\gamma}\right) + \frac{n_{A^-}}{\gamma}\ln\left(\frac{n_{H^+,\infty}}{K_a'}\right)\right]dy.\end{aligned} \tag{7}$$

Equation (7) is minimized using the variational formalism in the presence of the following constraints:

$$N = \int_{-h}^{y'} \frac{dy}{E(y, y')}, \tag{8}$$

$$N = \frac{1}{\sigma a^3} \int_{-h}^{-h+H} \phi(y) dy, \tag{9}$$

where N is the number of Kuhn monomers in every PE brush molecule.

Additionally, we have $\phi(y)$ related to the functions g and E as

$$\phi(y) = \sigma a^3 \int_{y}^{-h+H} \frac{g(y')dy'}{E(y, y')}. \tag{10}$$

This minimization procedure (please see Sachar *et al.* [33] for the step-by-step details of the procedure) eventually yields the final set of equations dictating the equilibrium of the system. We have taken $p = 1$ corresponding to the case of the fully flexible PE chain. These equations are provided below:

$$n_{A^-} = \frac{K_a' \gamma}{K_a' + n_{H^+,\infty} \exp\left(-\gamma a^3 \frac{e\psi}{k_B T}\right)}, \tag{11}$$

$$\epsilon_0 \epsilon_r \left(\frac{d^2\psi}{dy^2}\right) + e(n_+ - n_- + n_{H^+} - n_{OH^-} - n_{A^-}\phi) = 0 \quad (-h \leqslant y \leqslant -h + H),$$

$$\epsilon_0 \epsilon_r \left(\frac{d^2\psi}{dy^2}\right) + e(n_+ - n_- + n_{H^+} - n_{OH^-}) = 0 \quad (-h + H \leqslant y \leqslant 0), \tag{12}$$

$$n_{\pm} = n_{\pm,\infty} \exp\left(\mp \frac{e\psi}{k_B T}\right), \tag{13}$$

$$n_{H^+} = n_{H^+,\infty} \exp\left(-\frac{e\psi}{k_B T}\right), \tag{14}$$

$$n_{OH^-} = n_{OH^-,\infty} \exp\left(\frac{e\psi}{k_B T}\right), \tag{15}$$

$$\begin{aligned}\phi(y) = \frac{\nu}{3\omega}\Bigg(\Bigg\{1 + \kappa^2\Bigg[\lambda - (y+h)^2 + \beta \frac{K_a' \gamma}{K_a' + n_{H^+,\infty} \exp\left(-\gamma a^3 \frac{e\psi}{k_B T}\right)} \psi \\ - \rho\left(1 - \frac{K_a'}{K_a' + n_{H^+,\infty} \exp\left(-\gamma a^3 \frac{e\psi}{k_B T}\right)}\right) \ln\left(1 - \frac{K_a'}{K_a' + n_{H^+,\infty} \exp\left(-\gamma a^3 \frac{e\psi}{k_B T}\right)}\right) \\ - \rho \frac{K_a'}{K_a' + n_{H^+,\infty} \exp\left(-\gamma a^3 \frac{e\psi}{k_B T}\right)} \ln\left(\frac{K_a'}{K_a' + n_{H^+,\infty} \exp\left(-\gamma a^3 \frac{e\psi}{k_B T}\right)}\right) \\ - \rho \frac{K_a'}{K_a' + n_{H^+,\infty} \exp\left(-\gamma a^3 \frac{e\psi}{k_B T}\right)} \ln\left(\frac{n_{H^+,\infty}}{K_a'}\right)\Bigg]\Bigg\}^{1/2} - 1\Bigg),\end{aligned} \tag{16}$$

$$E(y, y') = \frac{\pi}{2N} \sqrt{(y' + h)^2 - (y + h)^2}, \tag{17}$$

$$(q_{\text{net}})_{H=H_0} = 0, \tag{18}$$

$$q_{\text{net}} = \frac{e}{\sigma} \int_{-h}^{0} (n_+ - n_- + n_{H^+} - n_{OH^-} - \phi n_{A^-}) dy, \tag{19}$$

$$g(y) = \frac{(y+h)}{\sigma N a^3}\Bigg[\frac{\phi(-h+H)}{\sqrt{H^2 - (y+h)^2}} - \int_{y}^{-h+H} \frac{d\phi(y')}{dy'} \frac{dy'}{\sqrt{(y'+h)^2 - (y+h)^2}}\Bigg]. \tag{20}$$

Equation (11) represents the expanded form of the mass action law. Equation (12) provides the equation governing the ψ distribution both inside ($-h \leqslant y \leqslant -h + H$) and outside ($-h + H \leqslant y \leqslant 0$) the brushes. Here we only consider the nanochannel bottom half ($-h \leqslant y \leqslant 0$). Equations (13)–(15) relate the ion number densities (n_i) to ψ and the corresponding bulk number density ($n_{i,\infty}$) through the Boltzmann distribution. Equation (16) expresses the monomer distribution profile in terms of the virial coefficients (characterizing the excluded volume interactions) ν and ω, parameters $\kappa^2 = \frac{9\pi^2\omega}{8N^2a^2\nu^2}$, $\rho = \frac{8a^2N^2}{3\pi^2}$, $\lambda = -\lambda_1\rho = -\lambda_1\frac{8a^2N^2}{3\pi^2}$ [λ_1 is the Lagrange multiplier yielded by the constraint expressed in Eq. (9)], $\beta = \frac{8N^2ea^5}{3\pi^2k_BT}$, and other variables (defined above). Equation (17) quantifies the local stretching of the PE brush. Equation (18), expressed in terms of the net unbalanced charge q_{net} [Eq. (19) provides an explicit expression for q_{net}], summarizes the condition for quantifying H_0 (the equilibrium brush height).

Finally, Eq. (20) provides the normalized distribution $g(y)$ for the end of the PE brush end [obtained from the condition $\int_{-h}^{-h+H} g(y')dy' = 1$]. The thermodynamics of the PE brush molecule, expressed as a coupled description of its configuration and the electrostatics of its induced EDL, is obtained by solving Eqs. (11)–(20). Of course, the differential equation expressing ψ [see Eq. (12)] is solved by first using Eqs. (11) and (13)–(15) to replace the ion number densities and Eq. (16) to replace the monomer distribution, and then employing the following boundary conditions:

$$\begin{aligned}(\psi)_{y=(-h+H)^-} &= (\psi)_{y=(-h+H)^+},\\ \left(\frac{d\psi}{dy}\right)_{y=(-h+H)^-} &= \left(\frac{d\psi}{dy}\right)_{y=(-h+H)^+},\\ \left(\frac{d\psi}{dy}\right)_{y=-h} &= 0,\\ \left(\frac{d\psi}{dy}\right)_{y=0} &= 0.\end{aligned} \tag{21}$$

The solution (see Ref. [33], which provides the step-by-step solution) eventually provides ϕ, ψ, $g(y)$, H_0, n_{A^-}, and n_i ($i = \pm$, H^+, OH^-), and therefore provides the complete equilibrium description of the system.

B. Electro-osmotic transport in brush-functionalized nanochannels: Theoretical model

Once the equilibrium brush configuration and the brush-induced EDL electrostatics have been obtained, we use this information to obtain the steady and fully developed EOS flow field in the PE-brush-grafted nanochannel. The fluid flow is described by the following equation:

$$\begin{aligned}&\eta\frac{d^2u}{dy^2} + eE(\Sigma_i n_i z_i) - \frac{\eta}{\kappa_d}u = 0 \quad (-h \leqslant y \leqslant -h + H_0),\\ &\eta\frac{d^2u}{dy^2} + eE(\Sigma_i n_i z_i) = 0 \quad (-h + H_0 \leqslant y \leqslant 0),\end{aligned} \tag{22}$$

in the presence of the boundary conditions expressed as

$$\begin{aligned}&(u)_{y=-h} = 0, \quad (u)_{y=(-h+H_0)^+} = (u)_{y=(-h+H_0)^-},\\ &\left(\frac{du}{dy}\right)_{y=0} = 0, \quad \left(\frac{du}{dy}\right)_{y=(-h+H_0)^+} = \left(\frac{du}{dy}\right)_{y=(-h+H_0)^-}.\end{aligned} \tag{23}$$

In the above equations, which consider the flow field only in the bottom half of the nanochannel (i.e., $-h \leqslant y \leqslant 0$), H_0 is the equilibrium brush height, η is the dynamic viscosity of water, E is the applied axial electric field, u is the velocity field, n_i and z_i are the number density distribution and valence of ion i ($i = \pm, H^+, OH^-$; "+" and "−" denote the cations and anions of the electrolyte), respectively, and η/κ_d represents the per unit volume drag coefficient. Here, following the analysis of de Gennes [57] and Freed and Edwards [58], one can express

$$\kappa_d = a^2/\phi^2 = a^2\left(\frac{H_0}{\sigma a^3 N\bar{\phi}}\right)^2 \tag{24}$$

and

$$\bar{\phi} = \frac{\phi H_0}{\sigma a^3 N}. \tag{25}$$

In the above equations, a is the PE brush Kuhn length, N is the number of monomers of a brush molecule, ϕ is the monomer distribution profile, and σ is the PE-brush-grafting density (please see [17,34] for more details). The augmented SST analysis provides an expression for the equilibrium brush height H_0, monomer distribution ϕ, brush-end distribution $g(y)$, and also relates n_i to the electrostatic potential ψ through the Boltzmann distribution (please see the previous section). This information closes Eqs. (22) and (23), which when solved yield the velocity distribution for the EOS transport in nanochannels with uncharged walls but grafted with backbone-charged, *p*H-responsive PE brushes. These velocity profiles are compared with those obtained for charged, brush-free nanochannels. The second equation of Eq. (22), valid for $-h < y < 0$, and the first and third conditions of Eq. (23) describe the EOS transport in such brush-free nanochannels having the same equivalent (bare-wall) surface charge density ($\sigma_{c,eq}$) as that of the corresponding brush-grafted nanochannels. We can write

$$\sigma_{c,eq} = -e\int_{-h}^{-h+H_0} \phi n_{A^-} dy, \tag{26}$$

where n_{A^-} is expressed in Eq. (11).

III. RESULTS AND DISCUSSIONS

We consider brush-grafted nanochannels with small ($\ell = 60$ nm) and large ($\ell = 10$ nm) grafting densities. Here, ℓ is the lateral separation between the grafted brushes with $\ell = 1/\sqrt{\sigma}$. $\sigma_{c,eq}$ of the brush-free nanochannels (defined above) vary depending on the brush-grafted nanochannels against which their results are compared. Figure 2 compares the velocity profiles for the brush-grafted and the corresponding (i.e., with identical charge content) brush-free nanochannels, revealing three key issues. First, the channel centerline maximum velocity for the brush-grafted nanochannel ($u_{\max,B}$) is always larger than that of the corresponding brush-free nanochannel ($u_{\max,NB}$). Second, an increase in salt concentration, in general, increases the ratio $u_r = u_{\max,B}/u_{\max,NB}$ for a given $p\mathrm{H}_\infty$ and ℓ. These two results signify the massive velocity enhancement effect of the brushes caused by the localization of the EOS body force away from the location of the wall-imparted drag force. For the brush-free nanochannels, the EDL and hence the EOS body force are localized at the same location as the wall-induced drag [see Fig. 1(a)] and hence such augmentation in the velocity field is not possible. For a larger salt concentration, the EDL is thinner. Therefore, this effect of the EDL localization becomes even stronger. For a more diffuse EDL (corresponding to smaller salt concentration), the EDL will spread out to near-wall locations, nullifying this overall effect of the EDL localization. As a consequence, u_r is larger for a larger salt concentration (also see Fig. 3), with the exception of long brushes ($\ell = 10$ nm) at large salt concentration ($c_\infty = 10^{-2}$–10^{-1} M) and high $p\mathrm{H}_\infty$. The third important result in this context is the significant gradient in the velocity for the brush-grafted nanochannels for

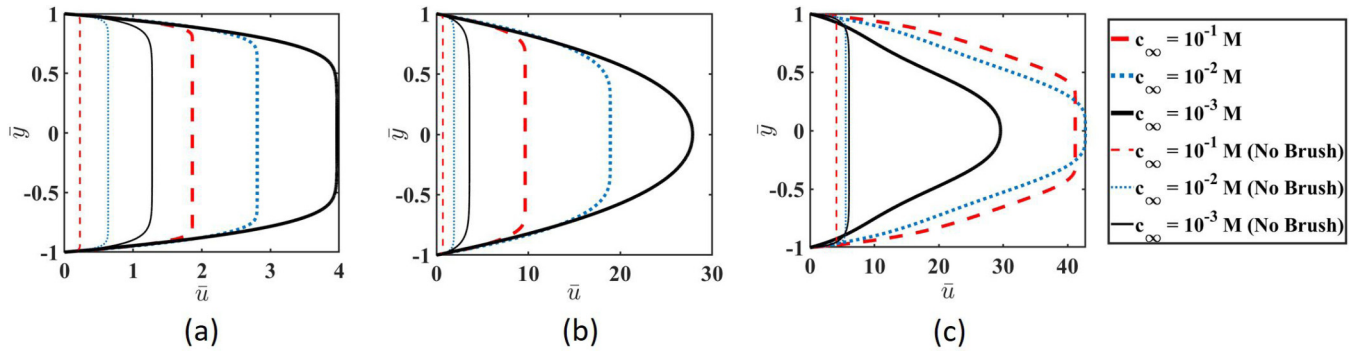

FIG. 2. Transverse variation of the nondimensional velocity profile $\bar{u}$ [$\bar{u} = \frac{u}{u_0}$, where $u_0 = (\frac{k_B T}{e})\frac{\epsilon_0 \epsilon_r E}{\eta}$ is the velocity scale, $k_B T$ is the thermal energy, ϵ_0 is the permittivity of free space, and ϵ_r is the relative permittivity of water] with bulk salt concentration c_∞ for the PE-brush-grafted nanochannel for (a) $p\mathrm{H}_\infty = 3$, $\ell = 60$ nm, (b) $p\mathrm{H}_\infty = 4$, $\ell = 60$ nm, and (c) $p\mathrm{H}_\infty = 3$, $\ell = 10$ nm. Here we consider the flow profiles for the equilibrium-brush-EDL configurations (see Sec. II A for the equations and Refs. [33,34] for the figures) obtained using $N = 400$, $h = 100$ nm, $a = 1$ nm (Kuhn length), $k_B = 1.38\times10^{-23}$ J K^{-1}, $T = 298$ K, $e = 1.6\times10^{-19}$ C (electronic charge), $\epsilon_0 = 8.8\times10^{-12}$ Fm^{-1}, $\epsilon_r = 79.8$, $\gamma a^3 = 1$, $pK_a = 3.5$, $\nu = 0.5$, $\omega = 0.1$. $pK_w = 14$, $pOH_\infty = pK_w - p\mathrm{H}_\infty$, $c_{+,\infty} = c_\infty$, $c_{H^+,\infty} = 10^{-p\mathrm{H}_\infty}$, $c_{OH^-,\infty} = 10^{-pOH_\infty}$, and $c_{-,\infty} = c_\infty + c_{H^+,\infty} - c_{OH^-,\infty}$. The definitions of all the terms and parameters are provided in Sec. II A.

small ℓ or large $p\mathrm{H}_\infty$ (i.e., the conditions that cause a larger brush height; see [33,34]). The larger brush height imparting a drag over a larger distance from the wall enforces such a gradient in the originally pluglike EOS flow profile (always witnessed for the brush-free nanochannels).

In Fig. 3, we compare the ratio u_r (defined previously). The u_r profile confirms an extraordinary enhancement of the centerline velocities (or, equivalently, the generation of ultrafast water transport with $u_r > 10$ for several cases) for the brush-grafted nanochannels. Finally, in the inset of Fig. 3, we provide the ratio $Q_r = Q_B/Q_{NB}$ (where $Q_B = w\int_{-h}^{h} u_B dy$ and $Q_{NB} = w\int_{-h}^{h} u_{NB} dy$ are the volume flow rates in brush-grafted and brush-free nanochannels, w is the nanochannel width, and u_B and u_{NB} are the velocity fields in brush-grafted and brush-free nanochannels). Q_r also shows an equally impressive increase and can even become >10 for certain parameter choices. For the studied set of parameters, both u_r and Q_r show the maximum enhancement for the nanochannel ($h = 250$ nm) with very tall (corresponding to small ℓ and large $p\mathrm{H}_\infty$) PE brushes at intermediate salt concentration ($c_\infty = 10^{-2}$ M). Of course, for such very tall brushes (corresponding to $\ell = 10$ nm and $p\mathrm{H}_\infty = 4$) at large salt concentration, the effect of EDL localization is superseded by the corresponding decrease in the brush height

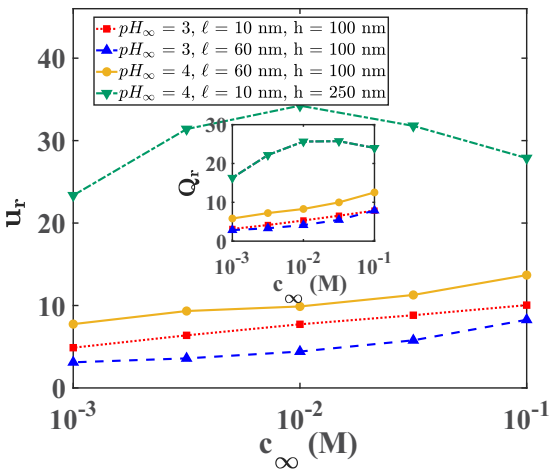

FIG. 3. Ratio of the maximum centerline velocities ($u_r = u_{\max,B}/u_{\max,NB}$) and volume flow rates ($Q_r = Q_B/Q_{NB}$) (inset) with c_∞ for different combinations of ℓ, h and, $p\mathrm{H}_\infty$. All other parameters are the same as those in Fig. 2.

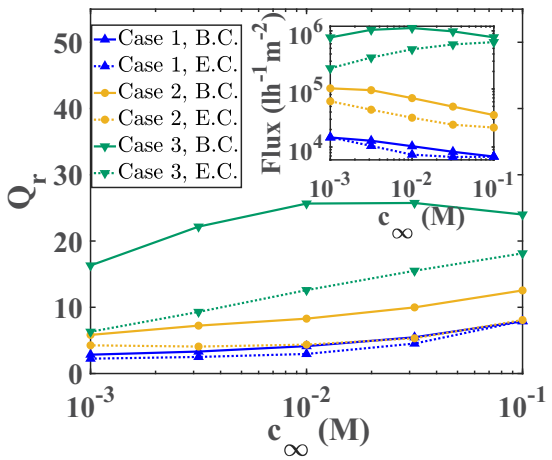

FIG. 4. Comparison of the ratio Q_r and the actual flux value (see the inset) between the present case (EOS transport in nanochannels grafted with backbone-charged brushes) and Ref. [26] (EOS transport in nanochannels grafted with end-charged brushes). We consider three cases in the main figure: Case 1: $p\mathrm{H}_\infty = 3$, $\ell = 60$ nm, $h = 100$ nm; Case 2: $p\mathrm{H}_\infty = 4$, $\ell = 60$ nm, $h = 100$ nm; Case 3: $p\mathrm{H}_\infty = 4$, $\ell = 10$ nm, $h = 250$ nm. In the inset, we compare the actual flux values for these three cases for an applied electric field $E = 500$ V cm^{-1}. In order to ensure that we are considering the same charge content of the PE brushes as the present case, the charge density for the end-charged PE brushes is considered to be $\sigma_{c,eq}$ [see the discussions following Eqs. (1) and (2) for the definition of $\sigma_{c,eq}$]. In the legend, B.C. and E.C. denote the cases of EOS transport in nanochannels grafted with backbone-charged (present case) and end-charged (Ref. [26]) brushes.

TABLE I. Flux values obtained from experimental studies on liquid transport in different nanofluidic systems.

Reference	Material	Pore space (nm)	Flux ($Lm^{-2}h^{-1}$)	Notes
Chong *et al.* [36]	GO membrane	1	0.3–9	This flux is calculated by using the capillary pressure in the GO membrane to be 6 bar (see Fig. 1(d) in [36]).
Zhou *et al.* [37]	GO membrane	0.86–0.92	0.015–0.15	This flux corresponds to a flux of 150 $gm^{-2}h^{-1}$ (see Fig. 1(f) in [37]).
Chong *et al.* [38]	GO membrane	0.7–1.4 ($\sim$1)	18–180	This flux is calculated by using the 10 bar pressure (Fig. 5 in [38]).
Liu *et al.* [39]	Nanostrand-channeled graphene oxide membranes	3–5	625–33000	See Fig. 3(a) and the result for flux at 1.5 MPa pressure in [39].
Han *et al.* [40]	Freestanding ultrathin rGO membrane	0.35	15–60	See Fig. 3(A) in [40].
Huang *et al.* [41]	Graphene oxide nanofiltration membrane intercalated by carbon nanotubes	0.5–2	40–60	We obtain this flux by multiplying the pressure (5 bar) with the flux data (see Table 1 in [41]).
Yang *et al.* [42]	Ultrathin graphene-based membrane	1.25–1.5	0.3–4	See Fig. 2(b) for water. The pressure is 1 bar (see the Methods section in [42]).
Tang *et al.* [43]	Polysulfone (PSf)-based mixed matrix membranes (MMMs) incorporated with two-dimensional boron nitride nanosheet (BNNS)	34.5–47.5	49.32–160.28	See Table 3 in [43]. The variation in the flux is due to the variation in the BNNS percentage content of the matrix.
Chen *et al.* [44]	Functionalized boron nitride (FBN) membranes	0.8–1.8	500–2800	See Fig. 3(b) in [44]. The value is for water. The experiments are conducted with a pressure of 1 bar. The variation in the flux is due to the variation in the FBN membrane thickness.
Surwade *et al.* [51]	Nanoporous single-layer graphene	$D \sim 1$	1.6×10^{6}–3.6×10^{6}	Initial flux given as 7×10^{-15} g s^{-1} atm^{-1} per pore with pressure difference of 50 atm. Flux given as $\sim1\times10^{6}$ $g.m^{-2}s^{-1}$.
Majumder *et al.* [52]	CNT	$D = 7$	3.6×10^{5}–1.8×10^{6}	See Table 1 in [52]. Calculated from velocities.
Whitby *et al.* [48]	Nanoscale carbon pipes	40–45	100–600	We have a maximum total water flow rate of 0.15 ml/min (see Fig. 4 in [48]). Number of pores in measured area (1 cm^2) = 1.07×10^{10}. Flow in a single pore = $\frac{0.15ml/min}{1.07\times10^{10}}$.
Yang *et al.* [44]	3.5 (PSS/PAH) coated 100 nm nanochannel membranes	100	0.1–1.5	Calculated from a flux value of 120 μ mol/min (See Fig. 6 in [44]).
Mathwig *et al.* [49]	Silicon nitride nanochannels	$2h = 130$	430–2585	Flow rate for a single channel is $\sim$28 pL/min (see Fig. 5 in [49]). Therefore, the flux is $\frac{28\times10^{-12}\times60}{(w\times2h)} = \frac{28\times10^{-12}\times60}{(5\times10^{-6})\times(130\times10^{-9})} \approx 2585$.

TABLE I. (*Continued.*)

Reference	Material	Pore space (nm)	Flux ($Lm^{-2}h^{-1}$)	Notes
Lee *et al.* [50]	Si chips	$2h = 163$	29.5	Flow rate for a single channel is ~400 fL/min (see Fig. 2 in [50]). Therefore, the flux is $\frac{400\times10^{-15}\times60}{(w\times2h)} = \frac{400\times10^{-15}\times60}{(5\times10^{-6})\times(163\times10^{-9})} \approx 29.5$.
Peng *et al.* [46]	Water permeation through protein membranes	$D \sim 1.7$	1000–8000	See Fig. 2(b) in [46].
Lee *et al.* [47]	Hydrophilic AAM	$D = 30$–100	1500–7000	Calculated using enhancement factors (see Table 2 in [47]).
	Current work	$2h = 200$–500	1450–1.12×10^{6}	Based on velocity.

(due to enhanced intersegmental screening). As a result, u_r and Q_r decrease in the range $c_\infty = 10^{-2}$–10^{-1} M. On the other hand, for other cases of not so tall brushes, u_r and Q_r increase monotonically with the salt concentration due to the dominating influence of the EDL localization effect.

In a recent study [26], we found an increase in the EOS velocity for nanochannels grafted with *end-charged* PE brushes. In Fig. 4, we compare Q_r and the flux of the present study with that of the study of Ref. [26]. We clearly find that the present case shows a larger value of Q_r and the flux. The previous study [26] considered a simplistic model of the PE brushes, where the brushes were described using the Alexander–de Gennes model, making the monomers uniformly distributed along the length of the brush. On the other hand, for the present case, we invoke a much more rigorous and realistic model where the brushes are described using the augmented SST [33]: this leads to a more appropriate distribution of the monomers where the monomer density is much larger at near-wall locations than at locations far away from the wall. In both the present and the previous studies [26], we attribute the increase in fluxes to the localization of the EDL charge density and the resulting EOS body force away from the wall (which is the location of the wall-induced drag force). Such localization of the EOS body force away from the location of wall-induced drag force leads to a much larger effect of the EOS body force causing such enhancement in the fluxes. In addition to this wall-induced drag, there is also the drag force resulting from the presence of the brushes themselves. The coefficient of the brush-induced drag force varies quadratically with the monomer distribution [see the discussions following Eq. (1)]. The simplistic model of our previous paper [26] assumes a uniform monomer distribution; hence it has the same number of monomers (and hence the same drag coefficient) at the near-wall location as well as the location where the EOS body force is localized. On the other hand, for the present case, the consideration of a much more rigorous and realistic monomer distribution implies that the monomer distribution is significantly larger at near-wall locations and hence significantly weaker at the location where the EOS body force is localized (i.e., at a location away from the wall). Accordingly, for the present case, at the locations where the EOS body force is effectively localized, the coefficient of the brush-induced drag force is significantly smaller. *In other words, for the present case, the EOS body force is localized at a location that is significantly deviated from the location of both the wall-induced and the brush-induced drag forces, while for the previous study [26], the EOS body force is localized at a location that is only deviated from the location of the wall-induced drag force but not from the location of the brush-induced drag force*. This, in turn, ensures a much larger value of the flux and Q_r for the present case as compared to our previous study [26].

Finally, in Fig. 5, we seek an answer to the following question: *How large is the flux in the brush-grafted nanochannels in the context of the large volume of studies on nanofluidic transport?* For that purpose, we try to compare the fluxes obtained for the brush-grafted nanochannels against the fluxes obtained in different nanochannel-based membranes, nanotubes, and nanofluidic systems (or isolated nanochannels). Most remarkably, the fluxes for the present case are remarkably high: we provide the results for different nanochannel height, brush height, and applied (and experimentally feasible) axial electric-field combinations (see Table I for all the relevant details) and find that the fluxes in the PE-brush-grafted nanochannels can be much larger than that for a wide variety of different nanofluidic or nanochannel-membrane systems. In fact, the fluxes are so large that they become comparable to (or slightly smaller than) the fluxes obtained in CNTs or nanoporous single-layer graphene known for extremely large flow velocities.

IV. CONCLUSIONS

To summarize, we have shown the attainment of the superfast EOS water transport in nanochannels by grafting nanochannels with *p*H-responsive, PE brushes. This enhancement makes the corresponding water flux much larger than the water flux obtained with most of the state-of-the-art nanofluidic and nanochannel-membrane systems. Such a finding establishes that brush functionalization, completely contrary to the general notion of the universal flow-reducing ability of the brushes, can serve as a strong promoter of the nanofluidic transport for a wide range of parameter values. Of course, for other parameter combinations (not studied here), the brush functionalization might retard the transport. The universal need to achieve enhanced transport and enhanced separation in nanochannels via energy efficient means cuts across the disciplines of fluid mechanics, materials

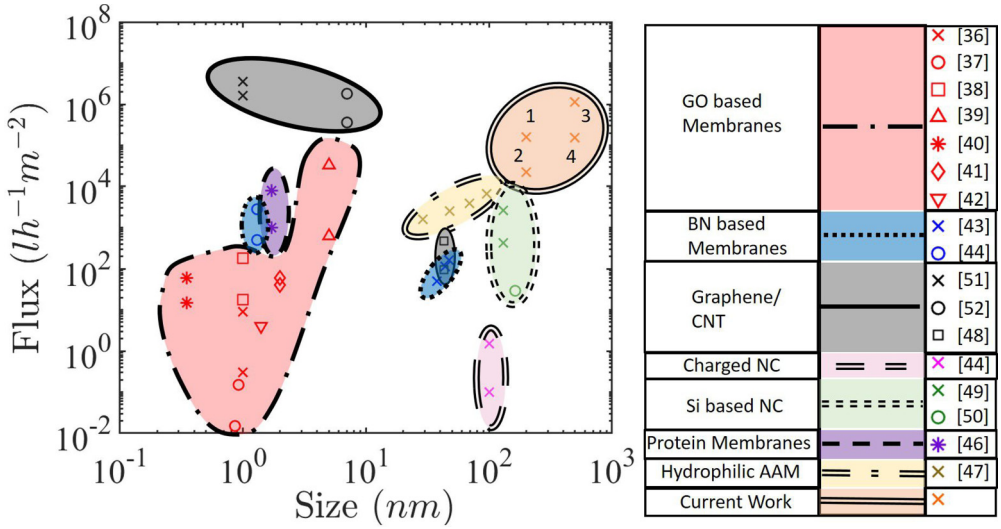

FIG. 5. Comparison of flux for various nanofluidic devices. Points 1 to 4 provide the results for the present case of a PE-brush-grafted nanochannel. Point 1: $pH_\infty = 3$, $c_\infty = 10^{-2}$ M, $\ell = 10$ nm, $h = 100$ nm, $E = 500$ V cm^{-1}; Point 2: $pH_\infty = 3$, $c_\infty = 10^{-3}$ M, $\ell = 10$ nm, $h = 100$ nm, $E = 100$ V cm^{-1}; Point 3: $pH_\infty = 4$, $c_\infty = 10^{-2}$ M, $\ell = 10$ nm, $h = 250$ nm, $E = 500$ V cm^{-1}; Point 4: $pH_\infty = 4$, $c_\infty = 10^{-3}$ M, $\ell = 10$ nm, $h = 250$ nm, $E = 100$ V cm^{-1}. For the current work, $\eta = 8.9\times10^{-4}$ Pa s, and all other parameters are the same as in Fig. 2. In Table I, we discuss the manner in which the fluxes for the different experimental studies (cited here) are calculated. GO: graphene oxide; BN: boron nitride; CNT: carbon nanotube; Si: silicon; AAM: anodized alumina membrane; NC: nanochannel.

science, biotechnology, nanotechnology, separation science, etc. We have achieved precisely that in this study by the facile means of PE brush functionalization.

ACKNOWLEDGMENT

This work has been supported by the U.S. Department of Energy Office of Science Grant No. DE-SC0017741.

[1] J. Gao *et al.*, Chem. Soc. Rev. **46**, 5400 (2017).
[2] J. C. T. Eijkel and A. van den Berg, Microfluid. Nanofluid. **1**, 249 (2005).
[3] A. R. Koltonow and J. X. Huang, Science **351**, 1395 (2016).
[4] Y. Zhu, K. Zhan, and X. Zhu, ACS Nano **12**, 908 (2018).
[5] R. Li *et al.*, Adv. Mater. **29**, 1702983 (2017).
[6] B. M. Venkatesan and R. Bashir, Nat. Nanotechnol. **6**, 615 (2011).
[7] B. N. Miles *et al.*, Chem. Soc. Rev. **42**, 15 (2013).
[8] R. C. Fang *et al.*, J. Am. Chem. Soc. **138**, 16372 (2016).
[9] M. Y. Liu *et al.*, Adv. Funct. Mater. **25**, 421 (2015).
[10] X. Huang *et al.*, Adv. Funct. Mater. **28**, 1801079 (2018).
[11] Z. Zhang, L. P. Wen, and L. Jiang, Chem. Soc. Rev. **47**, 322 (2018).
[12] M. Ali *et al.*, Anal. Chem. **83**, 1673 (2011).
[13] M. Ali *et al.*, J. Phys. Chem. C **117**, 18234 (2013).
[14] M. Ali *et al.*, ACS Nano **3**, 603 (2009).
[15] B. Yameen *et al.*, J. Am. Chem. Soc. **131**, 2070 (2009).
[16] B. Yameen *et al.*, Chem. Comm. **46**, 1908 (2010).
[17] G. Chen and S. Das, J. Appl. Phys. **117**, 185304 (2015).
[18] G. J. M. Bruin, J. P. Chang, R. H. Kuhlman, K. J. C. K. Zegers, J. C. Kraak, and H. Poppe, J. Chromatogr. A **471**, 429 (1989).
[19] E. N. Fung and E. S. Yeung, Anal. Chem. **67**, 1913 (1995).
[20] M. Monteferrante, L. Sola, M. Cretich, M. Chiari, U. Marini Bettolo Marconi, and S. Melchionna, J. Chem. Phys. **143**, 184907 (2015).
[21] Z. Zhang, C. Zuo, Q. Cao, Y. Ma, and S. Chen, Macromol. Theory Simul. **21**, 145 (2012).
[22] Y. Zuo, G. Wang, Y. Yu, C. Zuo, Z. Liu, D. Hu, and Y. Wang, Microfluid. Nanofluid. **17**, 923 (2014).
[23] R. Qiao, Langmuir **22**, 7096 (2006).
[24] S. P. Adiga and D. W. Brenner, Nano Lett. **5**, 2509 (2005).
[25] F. Tessier and G. W. Slater, Macromolecules **39**, 1250 (2006).
[26] G. Chen and S. Das, J. Phys. Chem. B **121**, 3130 (2017).
[27] G. Chen, H. S. Sachar, and S. Das, Soft Matter **14**, 5246 (2018).
[28] R. S. Maheedhara *et al.*, J. Phys. Chem. B **122**, 7450 (2018).
[29] R. S. Maheedhara *et al.*, Phys. Chem. Chem. Phys. **20**, 24300 (2018).
[30] S. Alexander, J. Phys. **38**, 983 (1977).
[31] P. G. de Gennes, J. Phys. France **37**, 1445 (1976).
[32] P. G. de Gennes, Macromolecules **13**, 1069 (1980).
[33] H. S. Sachar, V. S. Sivasankar, and S. Das, Soft Matter **15**, 559 (2019).
[34] H. S. Sachar, V. S. Sivasankar, and S. Das, Soft Matter **15**, 5973 (2019).
[35] S. Pennathur and J. G. Santiago, Anal. Chem. **77**, 6782 (2005).
[36] J. Y. Chong, B. Wang, and K. Li, Chem. Comm. **54**, 2554 (2018).
[37] K.-G. Zhou *et al.*, Nature (London) **559**, 236 (2018).
[38] J. Y. Chong *et al.*, J. Mem. Sci. **549**, 385 (2018).
[39] H. Liu, H. Wang, and X. Zhang, Adv. Mater. **27**, 249 (2015).
[40] Y. Han, Y. Jiang, and C. Gao, ACS Appl. Mater. Interface **7**, 8147 (2015).
[41] H. Huang *et al.*, Nat. Commun. **4**, 2979 (2013).

[42] Q. Yang *et al.*, Nat. Mater. **16**, 1198 (2017).
[43] C. Y. Tang *et al.*, Heliyon **5**, e01142 (2019).
[44] C. Chen *et al.*, Nat. Commun. **9**, 1902 (2018).
[45] M. Yang *et al.*, RSC Adv. **4**, 26729 (2014).
[46] X. Peng *et al.*, Nat. Nanotechnol. **4**, 353 (2009).
[47] K. P. Lee, H. Leese, and D. Mattia, Nanoscale **4**, 2621 (2012).
[48] M. Whitby *et al.*, Nano Lett. **8**, 2632 (2008).
[49] K. Mathwig, D. Mampallil, S. Kang, and S. G. Lemay, Phys. Rev. Lett. **109**, 118302 (2012).
[50] C. Lee, C. Cottin-Bizonne, A. L. Biance, P. Joseph, L. Bocquet, and C. Ybert, Phys. Rev. Lett. **112**, 244501 (2014).
[51] S. P. Surwade *et al.*, Nat. Nanotechnol. **10**, 459 (2015).
[52] M. Majumder *et al.*, Nature (London) **438**, 44 (2005).
[53] E. B. Zhulina and O. V. Borisov, Langmuir **27**, 10615 (2011).
[54] E. B. Zhulina and O. V. Borisov, J. Chem. Phys. **107**, 5952 (1997).
[55] E. B. Zhulina, V. A. Pryamitsyn, and O. V. Borisov, Pol. Sci. USSR **31**, 205 (1989).
[56] G. Chen and S. Das, RSC Adv. **5**, 4493 (2015).
[57] P. G. de Gennes, Macromolecules **9**, 594 (1976).
[58] K. F. Freed and S. F. Edwards, J. Chem. Phys. **61**, 3626 (1974).